Insertion Loss Analysis and Optimization of a Current Based Common-Mode Active EMI Filter

Jianrui Liu, *Graduate Student Member, IEEE*, Yechi Zhang, Dong Jiang, *Senior Member, IEEE*, Xuan Zhao, *Graduate Student Member, IEEE*, and Zicheng Liu, *Senior Member, IEEE*

***Abstract*—Active electromagnetic interference filter (AEF) is an effective method to handle common-mode (CM) electromagnetic interference (EMI). This article derives the accurate closed-loop transfer function of a feedback-type current-sensing current-compensating AEF. The attenuation factor (A_F) is defined in this article, identified as a critical parameter influencing the suppression performance of the AEF. For practical systems where the CM impedance exhibits capacitive behavior in high band, a method using impedance-optimized inductor is proposed to enhance the CM impedance environment of the feedback AEF. This enhancement raises A_F, thereby expanding the bandwidth of AEF and improving the suppression effects. An optimization strategy for insertion loss of the AEF is also proposed. The insertion loss is predicted and verified through experiments. The proposed AEF exhibits outstanding suppression performance in the range of 100 kHz to several MHz, achieving nearly 40 dB of CM EMI suppression in the region.**

***Index Terms*—Active electromagnetic interference filter (AEF), attenuation factor (AF), electromagnetic interference (EMI), impedance-optimized inductor, insertion loss, suppression effect.**

I. Introduction

With the development of high-power-density power electronic devices and wide-bandgap semiconductor devices, the voltage level and switching speed of power electronic converters have been significantly improved. High voltage jump and current jump are generated during the operation. The high *dv/dt* at the parasitic capacitors generates serious common-mode (CM) current, which flows in the CM loop of the system and affects the electromagnetic compatibility of the system. Electromagnetic interference (EMI) filter is a traditional method to suppress CM EMI [1], [2]. The inductor in passive EMI filter (PEF) carries the main power current while suppressing the CM current, resulting a large volume [3].

Four basic topologies of active EMI filter (AEF) were proposed in the 1990s, with the main idea being to sense EMI noise and then compensate by actively injecting compensation signals [4]. AEF has smaller volume and weight and better suppression effect in middle frequency band (several hundred of kHz to several MHz) compared to PEF. The suppression effect of AEF in high frequency band is very weak. AEF is always used in conjunction with PEFs, which can help to reduce the high frequency CM EMI [5]. The basic principle of several kinds of AEF was analyzed, and the hybrid EMI filter used in motor drive system was proposed which combines the advantages of PEF and AEF [5].

For motor drive systems, a feedforward voltage detection current compensation AEF based on motor CM impedance fitting is proposed [6]. This method eliminates the need for current sensors, but it imposes a higher requirement on motor impedance fitting. Another AEF designed for use in the motor ground circuit further reduces the number of AEF components, thus minimizing the overall size and weight [7].

Through a simplified transfer function analysis, the suppression effect of the AEF can be roughly estimated, but it is still not accurate enough. The accurate operational amplifier models and current sensor models of AEF were proposed, which makes it easier for the modeling and designing of AEF [8]. In [8], the closed-loop stability of AEF is analyzed, and the unstable resonance in high frequency is avoided by adding a resistor in the parasitic capacitance branch to the ground. The modeling of a differential-mode AEF in the specific situation was studied and the solution for the stability issue of this AEF was proposed in [9]. By changing the position of the zero pole with a parallel resistor in the feedback loop of the op-amp, the phase margin is increased, and the stability of the AEF is improved. However, this AEF is designed for relatively ideal boost converters with clear DM circuits. When applied to systems with higher power and more complex parasitic parameters, the situation may change. Besides, the impedance and phase characteristics of the noise source and load should be paid attention to in the analysis of AEF insertion loss, which plays a significant role in determining AEF performance [10].

In [11], a novel AEF approach based on inductance reuse was proposed. By increasing the inductance value of the primary winding of the current transformer (CT), the CT not only serves as an active sensing component but also functions as a passive inductor. This technique reduces the number of inductors in the hybrid filter, while simultaneously increasing the inductance value of the CT's primary side, with negligible changes in overall volume and weight. But, the passive CM impedance effect of the

Manuscript received 5 March 2024; revised 25 June 2024; accepted 25 July 2024. Date of publication 30 July 2024; date of current version 11 September 2024. Recommended for publication by Associate Editor R. C. Goswami. *(Corresponding author: Yechi Zhang.)*

Jianrui Liu, Dong Jiang, Xuan Zhao, and Zicheng Liu are with the State Key Laboratory of Advanced Electromagnetic Engineering and Technology, School of Electrical and Electronic Engineering, Huazhong University of Science and Technology, Wuhan 430074, China (e-mail: liujianrui@hust.edu.cn; jiangd@hust.edu.cn; zhaoxuan95@hust.edu.cn; liuzc@hust.edu.cn).

Yechi Zhang is with the School of Marine Electrical Engineering, Dalian Maritime University, Dalian 116026, China (e-mail: zhangyc@dlmu.edu.cn).

Color versions of one or more figures in this article are available at https://doi.org/10.1109/TPEL.2024.3435940.

Digital Object Identifier 10.1109/TPEL.2024.3435940

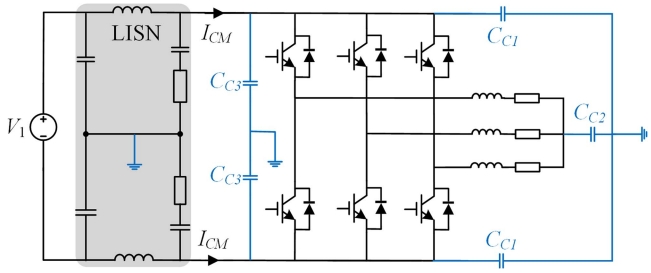

Fig. 1. Topology of motor drive system.

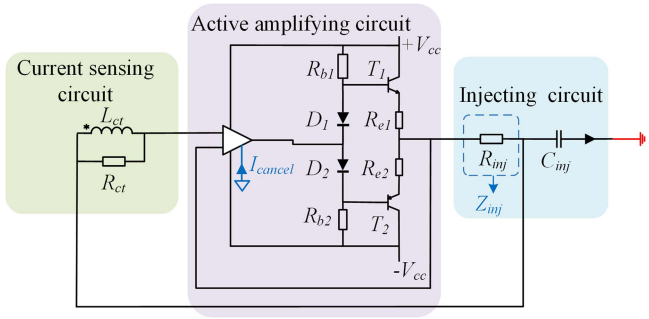

Fig. 2. Topology of current sensing current compensating AEF.

reused inductor is significantly weakened and no longer exhibits inductive impedance.

A novel integrated design of a filter has been developed that eliminates the need to separate CM and DM noise signals, providing suppression effects for both types [12]. Additionally, scholars have explored a CM AEF based on a neutral point construction. In this integrated design, the AEF shares a low-voltage dc power supply with the low-voltage tested equipment [13]. The suppression effect of a single AEF is somewhat limited, and studies have compared series and parallel structures of DM AEF cascaded configurations, revealing that the series structure exhibits superior suppression effects [14]. A more detailed comparative analysis has been proposed, showing that a series-parallel DM AEF with the voltage detection current compensation type in the prestage and the current detection current compensation type in the poststage achieves optimal suppression effects [15]. In [16], the insertion loss and loop gain of the DM AEF with series feedback configurations are analyzed in detail.

In addition, many recent studies on novel filter designs are mostly based on load systems with relatively clear CM or DM circuits, such as dc converters. However, the design of AEF for complex systems with higher power and more parasitic parameters often poses greater challenges. The CM loops of these systems are usually difficult to be modeled clearly. There are few studies on the insertion loss analysis and optimization strategy of AEF in such a system. Researches have been conducted on the application of current detection current compensation AEF in high-power converter platforms such as modular multilevel converters and solid-state transformers [17], [18]. However, the CM circuit construction is relatively ideal and cannot reflect the complex impact of parasitic parameters on the ground.

Integrated motor drive systems exhibit a compact layout of control circuits and motor units, resulting in a smaller volume and higher power density. However, this also introduces complex grounding, CM capacitance to the chassis, and severe EMI environments. The presence of various parasitic parameters complicates the paths for EMI. Fig. 1 shows a three-phase magnet synchronous motor powered through a dc–ac inverter. The motor windings and the load are equivalently modeled as resistance-inductance circuits. The chassis of the motor is grounded, and there are parasitic capacitors C_{C1} and C_{C2} between the motor neutral point and the dc bus of the switching devices and the ground. These capacitors provide a path for the circulation of CM currents. In general, the motor drive system incorporates a passive CM capacitor C_{C3} connected to the dc bus as a passive filter.

Building upon the application of AEF in integrated motor drive systems, this article conducts theoretical analysis and experimental validation of the insertion loss for feedback-type current detection current compensation AEF. This article proposes performance optimization strategies for the AEF.

The main contributions of this article are as follows.

1) The precise closed-loop transfer function of the feedback-type current detection current compensation AEF in the motor drive system is analyzed and derived. The insertion loss is predicted and verified through experiments.
2) The utilization of series-connected small CM inductors in AEF is proposed to alter the CM impedance environment of the motor drive system from capacitive to inductive, thereby enhancing the suppression effectiveness and bandwidth of the AEF. The feasibility of this approach was thoroughly analyzed and substantiated from a mechanistic standpoint.
3) The optimization method for the insertion loss curve of the AEF is introduced. This optimization can improve the frequency distribution of the insertion loss curve by changing the CM impedance matching mode between the AEF and the system.

The rest of this article as organized as follows. Section II provides a brief introduction to the basic components of the AEF and defines the functional modules within the closed-loop structure. Section III constitutes the core content of this article, deriving and predicting the closed-loop transfer function and insertion loss curve of the traditional AEF in electric drive systems. Additionally, it includes the derivation and analysis of the closed-loop transfer function of the system after the addition of series-connected small CM inductor. Predictions for the optimized insertion loss curve are made, and a method for optimizing the insertion loss curve is proposed. Section IV presents experimental results of the AEF in electric drive systems under different conditions, validating the results against theoretical predictions. Finally, Section V concludes this article.

II. Accurate Model of the CM Active Filter

AEF is mainly composed of detecting circuit, active amplifying circuit and injecting circuit. Fig. 2 shows the topology of current sensing current compensating AEF. A CT is designed as

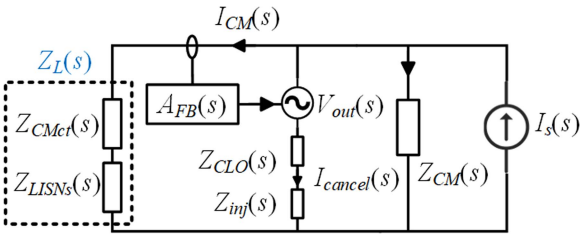

Fig. 3. CM closed-loop block diagram with feedback AEF.

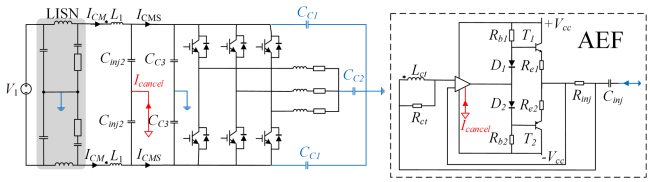

Fig. 4. Topology of motor drive system with feedback AEF.

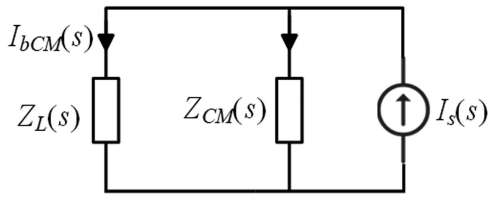

Fig. 5. CM model of motor drive system.

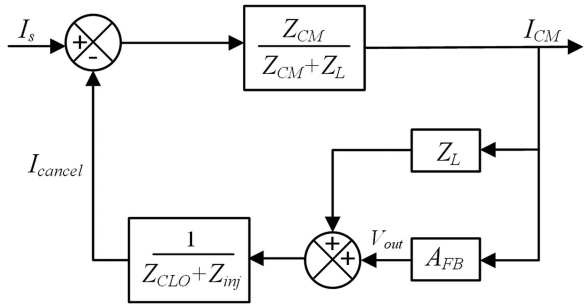

Fig. 6. CM closed-loop signal flow diagram of system.

the current sensing circuit. The primary windings are connected in series with the main circuit and the secondary winding $L_{\rm ct}$ induces current for the amplification. The active amplifying circuit is composed of operational amplifier (op-amp) and push-pull amplifier circuit. The injecting circuit consists of a resistor and a capacitor.

The simplified CM closed-loop block diagram of the feedback AEF based system is shown in Fig. 3.

$Z_{\rm LISNs}$ represents the equivalent CM impedance of LISNs. $Z_{\rm CMct}$ represents the equivalent impedance of the primary windings of CT caused by residual magnetic flux within the magnetic core [10].

In the analysis of the feedback configuration, $Z_{\rm LISNs}$ and $Z_{\rm CMct}$ occupy the same position in the block diagram analysis. Therefore, for the sake of simplicity in expression, we can define $Z_{\rm L}$ as the sum of $Z_{\rm LISNs}$ and $Z_{\rm CMct}$

$$Z_L(s) = Z_{\rm LISNs}(s) + Z_{\rm CMct}(s). \tag{1}$$

$A_{\rm FB}$ represents the transfer function from sensed CM current $I_{\rm CM}$ to the AEF output voltage $V_{\rm out}$, derived as follows:

$$A_{\rm FB}(s) = \frac{V_{\rm out}}{I_{\rm sense}} = G_{\rm ct} A_{\rm VOP}. \tag{2}$$

$G_{\rm CT}$ stands for the relationship between the sensed CM current and the output voltage. $A_{\rm VOP}$ represents the voltage gain of the entire active amplifying circuit. $Z_{\rm CLO}$ represents the closed-loop output impedance of the whole amplifying circuit. $Z_{\rm inj}$ represents the impedance of $R_{\rm inj}$ of injecting circuit. In this article, the AD826 operational amplifier is used for its broadband high-speed performance. FZT692B and FZT792A are used as the complementary triodes. $R_{\rm ct}$ is 200 Ωand $R_{\rm inj}$ is 20 Ω. The turn ratio of the CT is unity. The precise modeling of detection circuit and amplifier circuit has been studied in detail, so this article will not go into details [9].

III. Derivation of Closed-Loop Transfer Function in Motor Drive System

This section analyzes the closed-loop transfer function of the feedback AEF structure in application systems and further explores the optimization of its insertion loss. The motor drive system topology considering CM parasitic parameters and the current-based feedback-type AEF is shown in Fig. 4. The primary winding of CT connected in series with the main circuit is denoted as L_1. AEF detects CM currents on the dc bus side through CT, generates compensation signals, and feeds them back to the injection detection point, thereby achieving suppression of CM EMI on the bus side of the electric drive system.

When the AEF is not powered and current injection loop is disconnected, the simplified CM model of the motor drive system is depicted in Fig. 5. In this scenario, only the effect of equivalent impedance of the primary windings of CT in the AEF is considered. The Norton equivalent circuit is employed to represent the CM noise source of the motor drive system. I_S represents the equivalent CM current source, and $Z_{\rm CM}$ represents the equivalent system CM impedance. This impedance is mainly influenced by the parasitic capacitors C_{C1} and C_{C2} to the chassis, as well as the passive CM capacitor C_{C3}, thus exhibiting capacitive characteristics.

And the relationship between the CM current detected on the dc side and the CM current source can also be determined as follows:

$$G_{b\rm CM} = \frac{Z_{\rm CM}}{Z_{\rm CM} + Z_L}. \tag{3}$$

According to the closed-loop block diagram of the system with AEF shown in Fig. 3, the closed-loop signal flow diagram can be derived in Fig. 6.

Through the computation of the closed-loop transfer function depicted in Fig. 6, the ratio between the detected current and the CM current source, with the added AEF, can be derived as

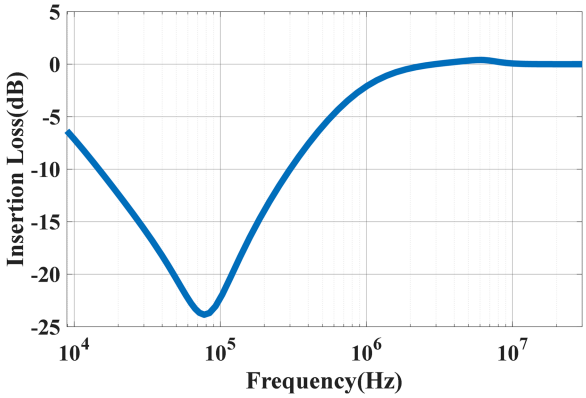

Fig. 7. Magnitude-frequency curve of AEF's insertion loss in theory.

follows:

$$G_{\mathrm{CM}} = \frac{\frac{Z_{\mathrm{CM}}}{Z_{\mathrm{CM}}+Z_L}}{1+\frac{Z_{\mathrm{CM}}}{Z_{\mathrm{CM}}+Z_L}\cdot\frac{A_{\mathrm{FB}}+Z_L}{Z_{\mathrm{CLO}}+Z_{\mathrm{inj}}}}. \tag{4}$$

According to the above derivation, the insertion loss of AEF can be derived as follows:

$$G_{\mathrm{ins}} = \frac{G_{\mathrm{CM}}}{G_{b\mathrm{CM}}} = \frac{1}{1+\frac{Z_{\mathrm{CM}}}{Z_{\mathrm{CM}}+Z_L}\cdot\frac{G_{\mathrm{ct}}A_{\mathrm{VOP}}+Z_L}{Z_{\mathrm{CLO}}+Z_{\mathrm{inj}}}}. \tag{5}$$

From (5), it's evident that the EMI suppression capability of the AEF is primarily influenced by the current sensing stage and the gain of the operational amplifier circuit. When Z_L and Z_{CLO} are constants, increasing A_{FB} and reducing Z_{inj} result in higher amplitude of insertion loss and a more pronounced suppression effect for the feedback-type AEF.

Additionally, it is affected by the A_F, which reflects the relationship between the system's CM impedance on both sides of the AEF injection point. As shown in (6), A_F is defined as the attenuation factor of the AEF's closed-loop feedback

$$A_F = \frac{Z_{\mathrm{CM}}}{Z_{\mathrm{CM}}+Z_L}. \tag{6}$$

Based on the analysis provided earlier, the magnitude-frequency curve of the AEF's insertion loss can be calculated, as shown in Fig. 7. It is noticeable that within the frequency range of 9 kHz to 3 MHz, the AEF exhibits a certain level of insertion loss, capable of suppressing the system's CM EMI. However, there is no suppression effect in the high-frequency range beyond 3 MHz.

Due to the capacitive CM impedance characteristics of the system, the CM impedance at high frequency is very small, resulting in a greatly reduced attenuation factor A_F at high frequency. As seen from (5), the reduction of A_F will greatly weaken the inhibition effect of AEF.

Considering the application scenario where the system's CM impedance exhibits capacitive characteristics at high frequencies, this article introduces a method to enhance the system's CM impedance characteristics by adding a small inductor in series. This approach compensates the attenuation factor A_F by changing the CM impedance structure of the system, and then optimizes the insertion loss of AEF in high frequency band. This method significantly improves the bandwidth and strengthens the suppression effect in the high-frequency range. As illustrated in Fig. 8, a small-value inductor L_2 is connected in series after the compensation current injection point. This arrangement results in the restructured CM impedance of the system exhibiting inductive characteristics at high frequencies.

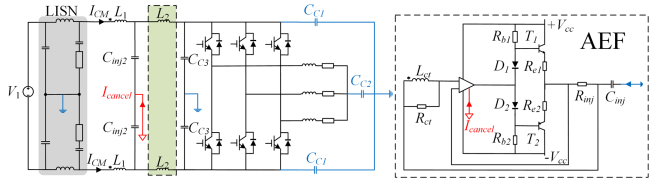

Fig. 8. Topology of motor drive system with corrected AEF.

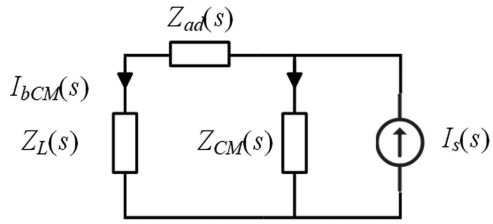

Fig. 9. Impedance optimization-based CM model of system.

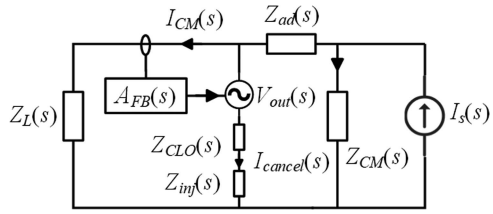

Fig. 10. CM closed-loop block diagram with corrected AEF.

When the AEF is not powered and current injection loop is disconnected, the simplified CM model of motor drive system is shown in Fig. 9. In contrast to Fig. 5, a small inductor L_2 is now in series. L_2 introduces an impedance term Z_{ad}, which is in parallel with Z_L and in series with the original system's CM impedance Z_{CM}.

The relationship between the CM current detected on the dc side and the CM current source can be determined as

$$G_{b\mathrm{CM}}{}' = \frac{Z_{\mathrm{CM}}}{Z_{\mathrm{CM}}+Z_L+Z_{ad}}. \tag{7}$$

With the designed current based AEF working, the simplified CM closed-loop block diagram of the system is shown in Fig. 10. In the logical block diagram, the position of the impedance-optimized inductor is situated between the current injection point and the system's CM impedance.

According to the closed-loop block diagram of the system, the closed-loop signal flow diagram can be derived in Fig. 11. Due to the distinct impedance relationships, the original CM current of the system and the compensation injection current have different division ratios. The term $(Z_{\mathrm{CM}}+Z_{ad})/Z_{\mathrm{CM}}$ within the closed-loop path serves as a correction factor for the compensation current injected into the system.

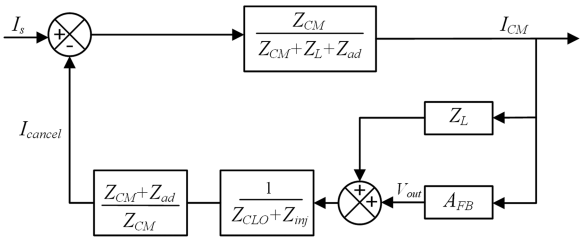

Fig. 11. CM closed-loop signal flow diagram with corrected AEF.

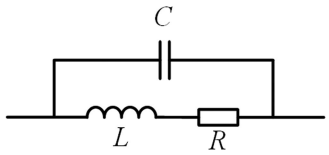

Fig. 12. Equivalent model of impedance optimization inductance considering high-frequency parasitic parameters.

TABLE I
PARAMETERS OF IMPEDANCE-OPTIMIZED INDUCTOR

	Turns	Equivalent inductance	Equivalent capacitance	Equivalent resistance
L_{ad1}	4	60 uH	600 pF	451 Ω
L_{ad2}	6	215 uH	580 pF	750 Ω
L_{ad3}	12	560 uH	460 pF	1500 Ω

By calculating the closed-loop transfer function in Fig. 11, the ratio of the detected current to the CM current source with AEF added can be obtained as follows:

$$G_{\mathrm{CM}}{}' = \frac{\frac{Z_{\mathrm{CM}}}{Z_{\mathrm{CM}}+Z_L+Z_{ad}}}{1+\frac{Z_{\mathrm{CM}}+Z_{ad}}{Z_{\mathrm{CM}}+Z_L+Z_{ad}}\cdot\frac{A_{\mathrm{FB}}+Z_L}{Z_{\mathrm{CLO}}+Z_{\mathrm{inj}}}}. \tag{8}$$

According to the above derivation, the insertion loss of AEF can be derived as follows:

$$G_{\mathrm{ins}}{}' = \frac{G_{\mathrm{CM}}{}'}{G_{b\mathrm{CM}}{}'} = \frac{1}{1+\frac{Z_{\mathrm{CM}}+Z_{ad}}{Z_{\mathrm{CM}}+Z_{\mathrm{LISNs}}+Z_{ad}}\cdot\frac{G_{\mathrm{ct}}A_{\mathrm{VOP}}+Z_L}{Z_{\mathrm{CLO}}+Z_{\mathrm{inj}}}}. \tag{9}$$

Under this circumstance, the closed-loop feedback factor $A_F{}'$ for the AEF can be expressed as

$$A_F{}' = \frac{Z_{\mathrm{CM}}+Z_{ad}}{Z_{\mathrm{CM}}+Z_L+Z_{ad}}. \tag{10}$$

It can be observed that the addition of the impedance-optimized inductor results in the closed-loop feedback factor $A_F{}'$ approaching 1. This maximizes the retention of the AEF feedback circuit's gain and theoretically enhances the AEF's CM EMI suppression capability.

In this article, CM inductors wound on ferrite magnetic cores are used as impedance-optimized inductors. The equivalent model of impedance optimization inductance considering high-frequency parasitic parameters is shown in Fig. 12. Table I gives the specific parameters of three different specifications of inductors measured by the vector network analyzer. Fig. 13 provides a physical comparison of these inductors.

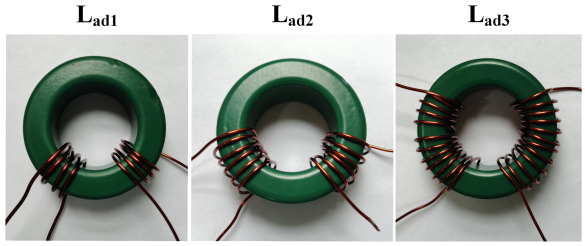

Fig. 13. Physical comparison of impedance-optimized inductors.

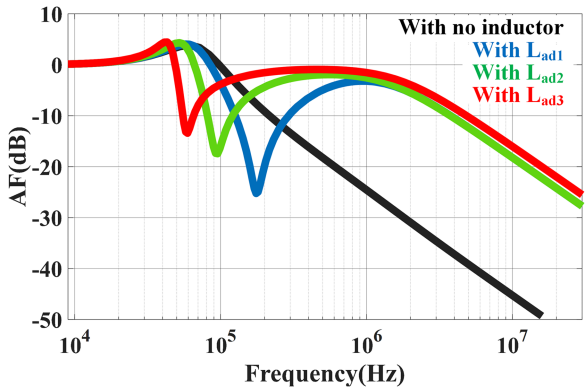

Fig. 14. Comparison of magnitude-frequency curve of A_F and $A_F{}'$.

Fig. 14 shows comparison of the magnitude-frequency characteristics of the closed-loop feedback factor A_F before and after impedance adjustment. The introduction of the impedance-optimized inductor alters the CM impedance behavior of the system, resulting in an expanded bandwidth for the influence factor. Prior to this adjustment, A_F decreases to -20 dB at 1 MHz, thereby restricting the impact of AEF closed-loop feedback beyond this frequency. After impedance optimization, the modified factor $A_F{}'$ reaches -20 dB at 10–20 MHz, which improving the effective working bandwidth of the closed-loop AEF significantly.

It's important to note that the local minimum of $A_F{}'$ in low frequency band is caused by the series resonance of the impedance-optimized inductor Z_{ad} with the parasitic CM capacitance to ground and the passive filter capacitor Z_{CM}. At the resonance point, the impedance is minimized, resulting in a resonant weakening point in the closed-loop feedback factor. The frequency and amplitude at this point can be adjusted by changing the value of the impedance-optimized inductor. This helps improve the suppression performance of the AEF near its low-frequency weakness, ensuring effective suppression of critical low-frequency harmonic CM EMI.

Based on (5) and (9), the insertion loss of the AEF can be calculated. The magnitude-frequency curve depicted in Fig. 15 illustrates the comparison of the theoretically calculated insertion loss of the AEF before and after incorporating the impedance-optimized inductor. This graph reflects the impact of impedance optimization on the AEF's insertion loss while operating. It can be observed that, following the adjustment of the system's impedance structure through the addition of the impedance-optimized inductor, the operational bandwidth

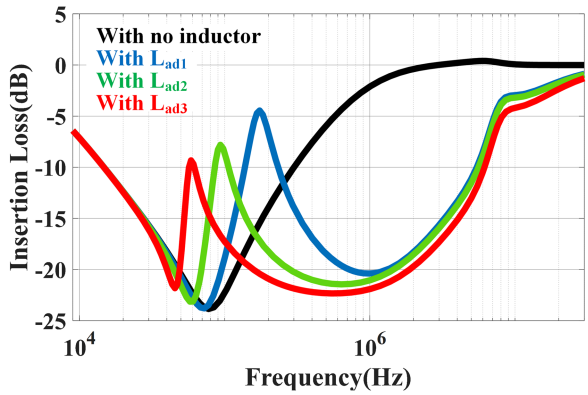

Fig. 15. Comparison of insertion loss of AEF with and without impedance-optimized inductor.

of the AEF increases from the original 3 MHz to around 8 MHz. Besides, the suppression effect at the MHz frequency is greatly enhanced. The dip in insertion loss observed in low frequency band is due to a decrease in $A_F{}'$ caused by resonance. Despite this, the AEF still exhibits a certain level of suppression at that point. This point can be adjusted by changing the impedance-optimized inductor.

IV. Verification of AEF Based on Impedance Optimization in Motor Drive System

This section primarily demonstrates the performance of the improved feedback-type AEF in an experimental motor system. The experiment focuses on a three-phase permanent magnet synchronous motor with a load. The motor is powered by a dc–ac inverter through a dc power supply. The dc-bus voltage during motor operation is 200 V, with a speed of 1200 revolutions per minute. The system operates with load at 550 W. A sinusoidal pulsewidth modulation technique is employed to generate modulation waves for motor drive, operating at a switching frequency of 10 kHz. The total parasitic CM capacitance of the electric drive system to ground has been measured to be around 6 nF. The value chosen for the CM filtering capacitor C_{C3} is 3.1nF. The experimental setup is illustrated in Fig. 16.

Fig. 17 shows a comparison of the CM EMI spectra in the motor drive system before and after the use of the traditional feedback-type AEF. The blue curve represents the system's CM EMI when the AEF is not in operation, while the red curve represents the system's CM EMI when the AEF is powered ON. The measured insertion loss of the traditional feedback-type AEF, calculated based on the blue and red dashed envelope lines, is compared to the predicted AEF insertion loss obtained through theoretical derivation in this article, as shown in Fig. 18. It can be observed that the traditional feedback-type AEF has a moderate effect in real motor drive systems, providing a CM suppression effect of only 10–20 dB in the frequency range of 9 kHz to 1 MHz, with almost no suppression effect above 1 MHz.

Under the current configuration, the system's CM impedance Z_{CM} exhibits capacitive characteristics, primarily attributed to the CM filtering inductor C_{C3} and the parasitic capacitors C_{C1}

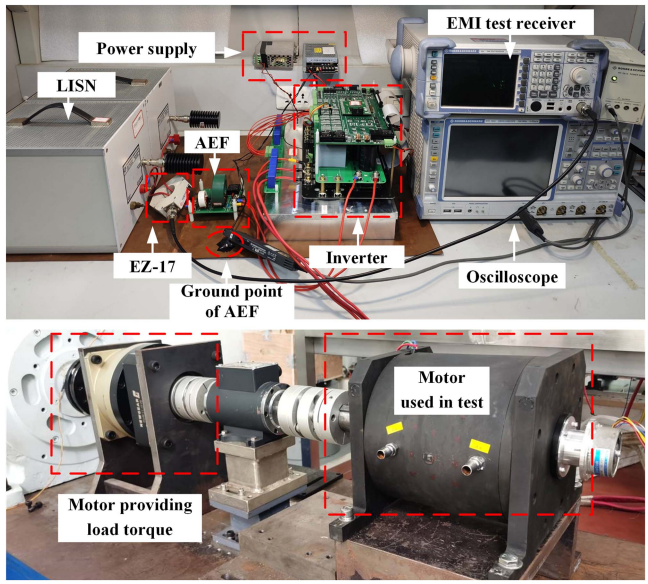

Fig. 16. Experimental setup.

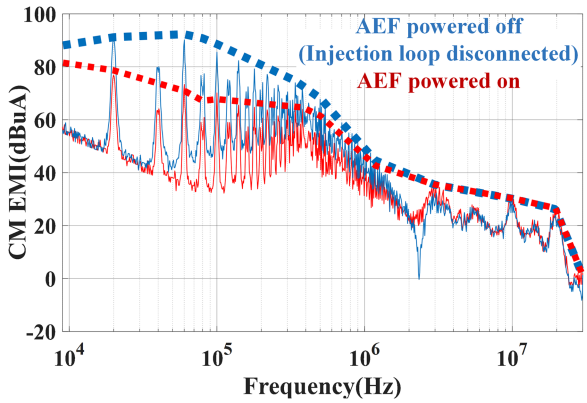

Fig. 17. Comparison of CM EMI with feedback AEF.

and C_{C2} from the motor to the chassis, as described in Section III. The analysis of the insertion loss of the AEF described by (5) indicates that the magnitude of the A_F for the closed-loop feedback is less than 1. In the high-frequency range, the capacitive nature of Z_{CM} in the A_F term tends to bring its magnitude closer to 0. This weakening effect influences the gain of the AEF feedback circuit and further contributes to the reduction in the magnitude of the AEF's insertion loss.

In order to reduce the attenuation effect of the A_F on the AEF's suppression performance, this article adopts the approach of serially connecting impedance-optimized inductors to improve the system's CM impedance structure. This method increases the magnitude of A_F within the high-frequency range, ultimately achieving an expansion of the AEF's bandwidth and enhancement of its suppression performance.

The study encompassed comparative experiments aimed at verifying the impact of the impedance-optimized inductor. This article utilized three different impedance-optimized inductors with varying numbers of turns and inductance values, namely L_{ad1}, L_{ad2}, and L_{ad3}. Their detailed parameters are provided in

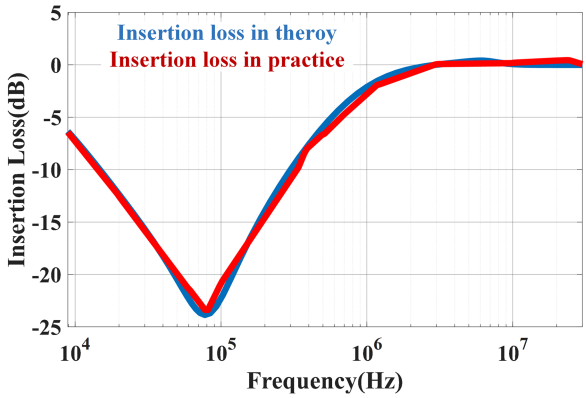

Fig. 18. Comparison of insertion loss in theory and in practice.

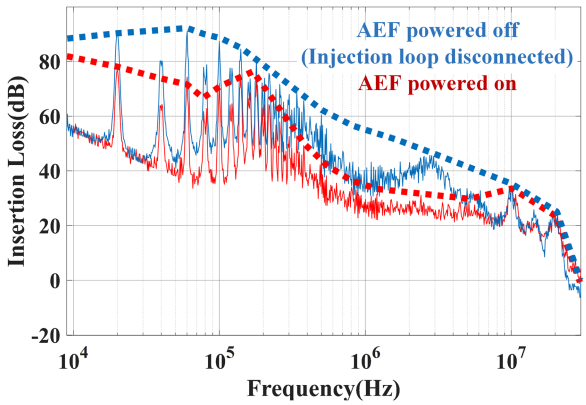

Fig. 19. Comparison of CM EMI with L_{ad1}-based AEF.

Section III. Using L_{ad1} as the impedance-optimized inductor, which has the minimum number of turns and inductance value, a spectrum comparison of the CM EMI on the system's dc bus side before and after the operation of the feedback-type AEF is shown in Fig. 19. The meanings of the curves are similar to those described earlier. It is evident that the effective operating bandwidth of the AEF has significantly increased, extending to nearly 10 MHz, with a maximum suppression effect of around 20 dB. This change is attributed to the adjustment of the system's impedance structure through the incorporation of the impedance-optimized inductor. Based on Fig. 19, the measured insertion loss of the AEF is obtained and compared to the predicted insertion loss from Section III, resulting in Fig. 20. It can be seen that these two curve fit closely.

Increasing the inductance value of the impedance-optimized inductor verifies its impact on the AEF's low-frequency insertion loss weakness. By sequentially using L_{ad2} and L_{ad3}, spectrum comparisons of the system's CM EMI before and after powering up the AEF are obtained, as shown in Figs. 21 and 23. The comparisons between the measured insertion loss of the AEF and the theoretical calculations are shown in Figs. 22 and 24, respectively, for these two scenarios. It can be observed that as the inductance value of the impedance-optimized inductor increases, the AEF's suppression effect enhances slightly and remains relatively high values in the frequency range of several hundred kHz to 10 MHz. The weakness in suppression at lower

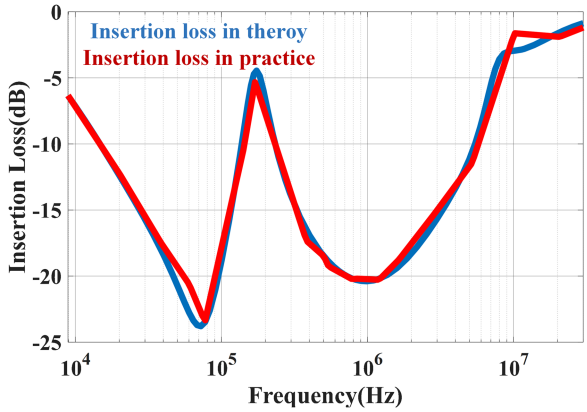

Fig. 20. Comparison of insertion loss in theory and in practice with L_{ad1}-based AEF.

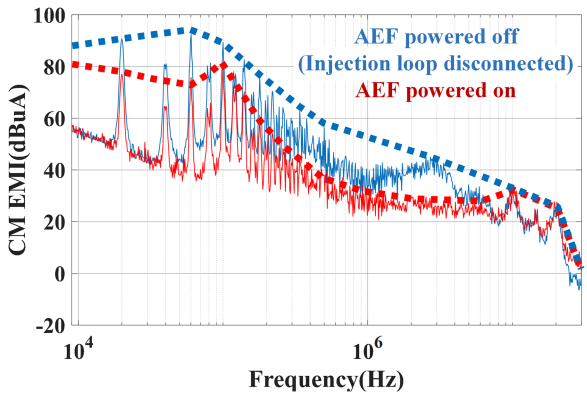

Fig. 21. Comparison of CM EMI with L_{ad2}-based AEF.

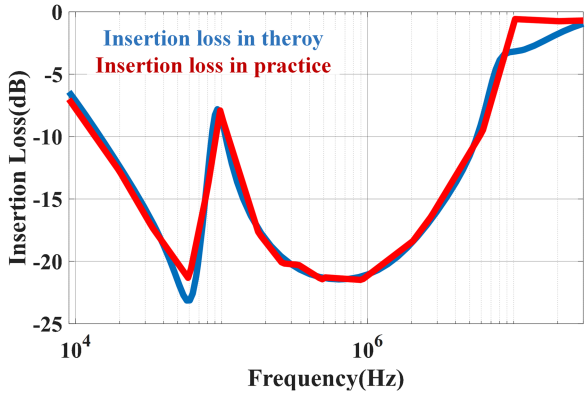

Fig. 22. Comparison of insertion loss in theory and in practice with L_{ad2}-based AEF.

frequencies shifts to a smaller frequency range, resulting in improved suppression. This, in turn, widens the effective suppression frequency range of the AEF. Table II gives the measured insertion loss values for different impedance-optimized inductors. From Figs. 22 and 24, it can be seen that the measured insertion loss closely matches the predicted insertion loss from theoretical calculations, validating the accuracy of the theoretical analysis and precise modeling presented in this article.

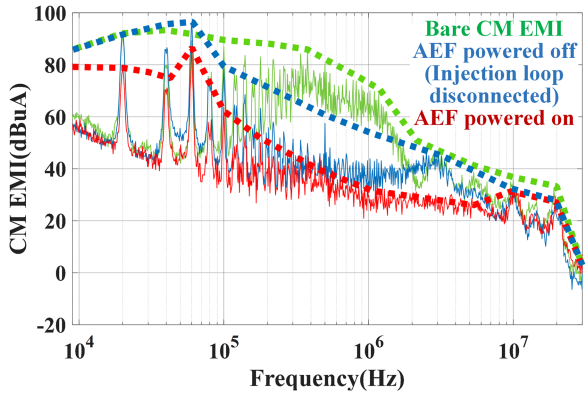

Fig. 23. Comparison of CM EMI with L_{ad3}-based AEF.

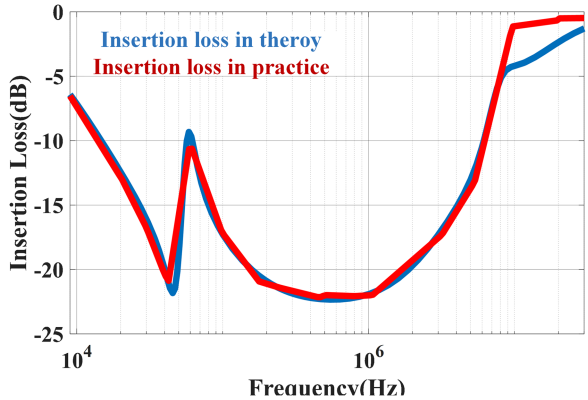

Fig. 24. Comparison of insertion loss in theory and in practice with L_{ad3}-based AEF.

TABLE II
INSERTION LOSS OF AEF WITH DIFFERENT LAD

	Turns	Equivalent inductance	resonance point	IL at this point	Max of IL
L_{ad1}	4	60 uH	180 kHz	–6 dB	–21 dB
L_{ad2}	6	215 uH	100 kHz	–8 dB	–22 dB
L_{ad3}	12	560 uH	60 kHz	–12 dB	–23 dB

By comparing these three optimized design cases, it can be concluded that the suppression capability and bandwidth of the AEF improve as the inductance value of the impedance-optimized inductor increases. In complex systems with varying parasitic capacitances to ground, the impedance-optimized inductor is an important design parameter that influences the suppression performance of the AEF. The optimized design recipe for AEF is shown in Fig. 25.

As shown in Fig. 25, this article includes the design guidelines for AEF. The general optimization design method of AEF should follow the following process: First, the CM impedance structure of the system should be concerned and its impedance characteristics should be measured. Precise models of AEF functional modules and impedance optimized inductors are also required. According to these, the closed-loop transfer function of AEF in the system can be derived, and the insertion loss curve of

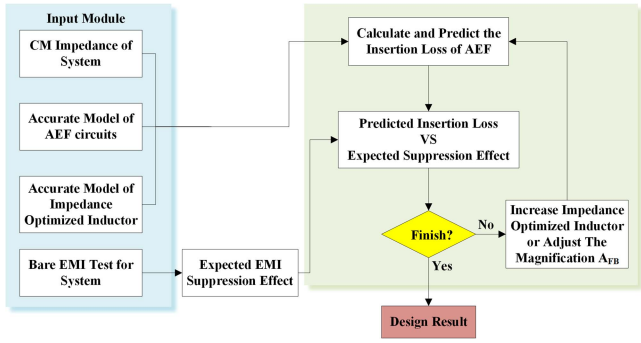

Fig. 25. Optimized design recipe for AEF.

AEF can be calculated and predicted. The original CM EMI of the system is measured, and the desired suppression effect of the filter is obtained according to the EMI standard that needs to be achieved. The designed AEF predicted insertion loss is compared with the filter suppression effect expected by the system. If the suppression requirement is met, the design result is obtained. If the requirements are not met, it is necessary to increase the inductance value of the impedance optimization inductor or adjust the total magnification A_{FB}, rededuce the AEF closed-loop transfer function and predict the insertion loss, and compare the desired suppression effect. This process is repeated until the design requirements are met.

Loop gain analysis is an important method for analyzing the closed-loop stability of AEF. Based on the CM closed-loop signal flow diagram with corrected AEF shown in Fig. 11, the loop gain $G_{\mathrm{loop}'}$ of the AEF can be derived as follows:

$$G_{\mathrm{loop}}{}' = \frac{Z_{\mathrm{CM}} + Z_{ad}}{Z_{\mathrm{CM}} + Z_L + Z_{ad}} \cdot \frac{A_{\mathrm{FB}} + Z_L}{Z_{\mathrm{CLO}} + Z_{\mathrm{inj}}}. \tag{11}$$

Taking the design of an AEF with impedance-optimized inductors based on L_{ad3} as an example, the precise expression for the loop gain of the corrected AEF can be calculated in MATLAB, and its Bode diagram is predicted and drawn as shown in Fig. 26. It can be observed that the phase margin is approximately 100 degrees, indicating that the AEF feedback system is stable. The optimized AEF design proposed in this article avoids high-frequency unstable resonance.

As shown in Fig. 4, I_{CMS}, the total CM current to ground in the system can be measured on the dc bus near the motor side at the AEF injection point. In theory, a well designed feedback-type AEF can inject a compensating current identical to I_{CMS} to reduce the CM EMI current measured at the LISN side. Using an oscilloscope to measure the whole CM current to the ground I_{CMS} and the compensating current I_{cancel} of the feedback AEF when using L_{ad3} as impedance-optimized inductor, their time-domain waveforms are shown in Fig. 27. It can be seen that the compensating current is approximately equal in magnitude and direction to I_{CMS}. I_{CMS} contains a low-frequency component at 60 kHz, and the compensating current exhibits some low-frequency distortion at this frequency point compared to I_{CMS}, indicating a relatively weaker EMI suppression effect at 60 kHz, which can be verified in Fig. 24.

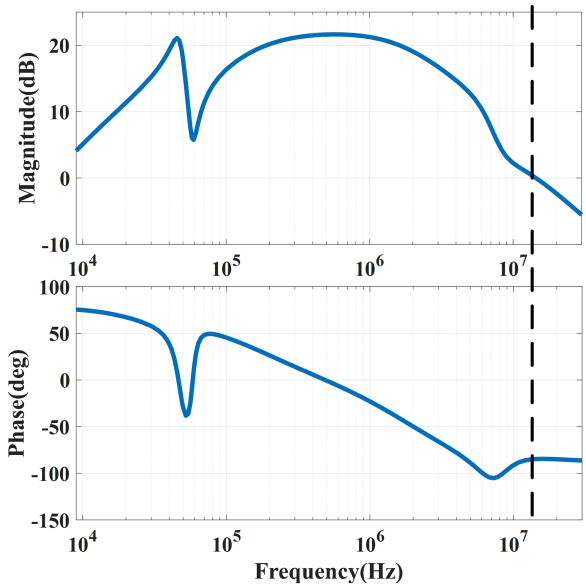

Fig. 26. Bode diagram of the loop gain of the corrected AEF.

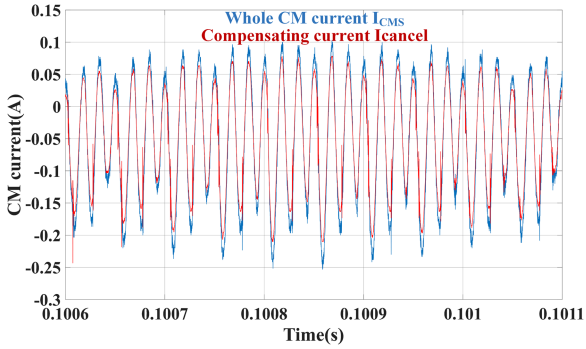

Fig. 27. Comparison of whole CM current and compensating current.

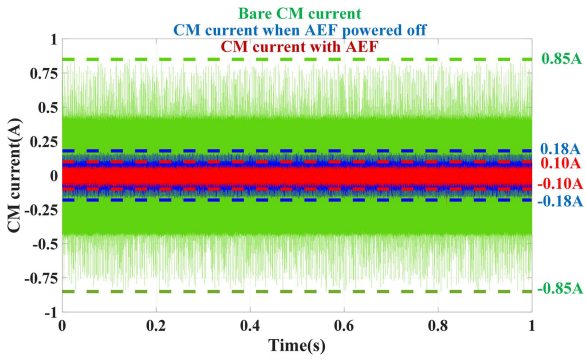

Fig. 28. Comparison of bare CM current and reduced CM current.

Fig. 28 presents a time-domain waveform comparison of the system's CM current. The green curve represents bare CM current of the system. With the impedance-optimized inductor L_{ad3} added, the blue curve represents CM current when AEF is powered off and disconnected. The red curve represents the CM current using this AEF. After implementing the feedback AEF, there is a further suppression in the time-domain waveform of the system's CM current compared to that with only passive inductor L_{ad3}.

Since both the integrated CT within the main circuit and the impedance-optimized inductor also function as passive filters when the AEF is not powered on, a certain level of CM EMI suppression is still apparent even when the AEF is not in operation. This contrast is evident when compared to the original CM EMI. In order to better compare the suppression effect of the active part of AEF alone, this passive effect has not been accounted for in the analytical calculations of the insertion loss in this article. Considering this passive suppression effect of feedback AEF, the green curve in Fig. 23 shows the bare CM EMI. The comparison between the green and blue envelope lines indicates that the AEF's inherent parallel structure, along with passive inductors, provides a suppression effect of around 10–20 dB between several hundred kHz and 2 MHz. Combining the suppression effects of these two components, the effective suppression bandwidth of the feedback-type current AEF based on impedance-optimized inductors, as proposed in this article, can reach 20 MHz, achieving approximately 40 dB of CM suppression in the range from 100 kHz to 1 MHz.

V. Conclusion

This article proceeds to analyze and derive the precise transfer function and insertion loss of feedback-type current-based CM AEF closed-loop circuit, based on real application systems. Given the intricate challenges stemming from complex grounding and the varied parasitic parameters inherent for the performance of AEF in capacitive CM impedance systems, this article introduces an innovative feedback-type current-based AEF approach based on CM impedance optimization. This technique achieves an extension of the operational bandwidth of AEF and enhances its noise reduction effects by bolstering the attenuation factor A_F. The proposed integrated AEF exhibits outstanding suppression performance in the range of 100 kHz to several MHz, achieving nearly 40 dB of CM EMI suppression.

By manipulating the value of the impedance-optimized inductor, the frequency spectrum of AEF insertion loss can be tailored to specific requirements. This article conducted experiments with feedback-type AEF in practical motor drive systems, thereby confirming the correctness of the proposed insertion loss theory calculations and optimization strategies.

The contribution of this article lies in introducing a generalized impedance adjustment method tailored for the application of AEF in integrated practical systems characterized by substantial CM parameters. This article provides a solid theoretical foundation and a comprehensive derivation analysis for this method by closed-loop transfer function analysis.

References

[1] G. L. Skibinski, R. J. Kerkman, and D. Schlegel, "EMI emissions of modern PWM AC drives," *IEEE Ind. Appl. Mag.*, vol. 5, no. 6, pp. 47–80, Nov./Dec. 1999.

[2] K. Mainali and R. Oruganti, "Conducted EMI mitigation techniques for switch-mode power converters: A survey," *IEEE Trans. Power Electron.*, vol. 25, no. 9, pp. 2344–2356, Sep. 2010.

[3] B. Narayanasamy and F. Luo, "A survey of active EMI filters for conducted EMI noise reduction in power electronic converters," *IEEE Trans. Electromagn. Compat.*, vol. 61, no. 6, pp. 2040–2049, Dec. 2019.
[4] L. LaWhite and M. F. Schlecht, "Design of active ripple filters for power circuits operating in the 1–10 MHz range," *IEEE Trans. Power Electron.*, vol. 3, no. 3, pp. 310–317, Jul. 1988.
[5] S. Wang, Y. Y. Maillet, F. Wang, D. Boroyevich, and R. Burgos, "Investigation of hybrid EMI filters for common-mode EMI suppression in a motor drive system," *IEEE Trans. Power Electron.*, vol. 25, no. 4, pp. 1034–1045, Apr. 2010.
[6] Y. Zhang, Q. Li, and D. Jiang, "A motor CM impedance based transformerless active EMI filter for DC-side common-mode EMI suppression in motor drive system," *IEEE Trans. Power Electron.*, vol. 35, no. 10, pp. 10238–10248, Oct. 2020.
[7] Y. Zhang and D. Jiang, "An active EMI filter in grounding circuit for DC side CM EMI suppression in motor drive system," *IEEE Trans. Power Electron.*, vol. 37, no. 3, pp. 2983–2992, Mar. 2022, doi: 10.1109/TPEL.2021.3110144.
[8] Y. Chu, S. Wang, Q. Wang, and R. Goswami, "Modeling and stability analysis of active/hybrid common-mode EMI filters for DC/DC power converters," in *Proc. IEEE Energy Convers. Congr. Expo.*, 2015, pp. 247–254.
[9] R. Goswami and S. Wang, "Modeling and stability analysis of active differential-mode EMI filters for AC/DC power converters," *IEEE Trans. Power Electron.*, vol. 33, no. 12, pp. 10277–10291, Dec. 2018.
[10] E. Mazzola, F. Grassi, and A. Amaducci, "Enhanced circuit model for insertion loss prediction of active EMI filters considering non-ideal parameters," in *Proc. Int. Symp. Electromagn. Compat.*, 2020, pp. 1–5.
[11] L. Dai, W. Chen, X. Yang, M. Zheng, Y. Yang, and R. Wang, "A multifunction common mode choke based on active CM EMI filters for AC/DC power converters," *IEEE Access*, vol. 7, pp. 43534–43546, 2019.
[12] Y. Zhou et al., "A new integrated active EMI filter topology with both CM noise and DM noise attenuation," *IEEE Trans. Power Electron.*, vol. 37, no. 5, pp. 5466–5478, May 2021.
[13] Y. Zhou et al., "A novel neutral point-based active EMI filter for common mode noise attenuation," *IEEE Trans. Power Electron.*, vol. 37, no. 9, pp. 10081–10085, Sep. 2022.
[14] R. Goswami and S. Wang, "Investigation of multiple feedback active filter configurations for differential mode (DM) electromagnetic interference (EMI) noise in AC/DC converter applications," in *Proc. 43rd Annu. Conf. IEEE Ind. Electron. Soc.*, 2017, pp. 7018–7023.
[15] Y. Zhou, W. Chen, and X. Yang, "Investigation of cascade connection method to improve the insertion loss of DM active EMI filters," *IEEE J. Emerg. Sel. Topics Power Electron.*, vol. 10, no. 1, pp. 1084–1094, Feb. 2022.
[16] R. Goswami and S. Wang, "Investigation and modeling of combined feedforward and feedback control schemes to improve the performance of differential mode active EMI filters in AC–DC power converters," *IEEE Trans. Ind. Electron.*, vol. 66, no. 8, pp. 6538–6548, Aug. 2019.
[17] J. Liu, D. Jiang, W. Sun, Y. Zhang, and J. Chen, "A common-mode active EMI filter design for modular multilevel converters," in *Proc. IEEE 1st Int. Power Electron. Appl. Symp.*, 2021, pp. 1–5.
[18] D. Jiang, Z. Wang, W. Chen, J. Liu, and W. Sun, "Common-mode electromagnetic interference mitigation for solid-state transformers," *Chin. J. Elect. Eng.*, vol. 8, no. 3, pp. 22–36, 2022.

Jianrui Liu (Graduate Student Member, IEEE) was born in Shanxi, China, in 1999. He received the B.S. and M.S. degrees in electrical engineering from the Huazhong University of Science and Technology, Wuhan, China, in 2021 and 2024, respectively.

His main research interests include electromagnetic interference, active EMI filter, and electromagnetic compatibility.

Yechi Zhang received the B.S. degree in electrical engineering and automation from North China Electric Power University, Beijing, China, in 2014, and the Ph.D. degree in electrical engineering from the Huazhong University of Science and Technology, Wuhan, China, in 2021.

He is currently a Lecturer with Dalian Maritime University, Dalian, China. His research interests include electromagnetic interference /electromagnetic compatibility in power converters and EMI filter design.

Dong Jiang (Senior Member, IEEE) received the B.S. and M.S. degrees in electrical engineering from Tsinghua University, Beijing, China, in 2005 and 2007, respectively. He is currently working toward the Ph.D. degree with the Center for Power Electronics Systems, Virginia Tech, Blacksburg, VA, USA, in 2007, and was transferred, with his advisor in 2010, to the University of Tennessee, Knoxville, TN, USA, where he received the Ph.D. degree in power electronics and motor drives in 2011.

He was with the United Technologies Research Center, East Hartford, CT, USA, as a Senior Research Scientist/Engineer, from 2012 to 2015. He has been a Professor with the Huazhong University of Science and Technology, Wuhan, China, since 2015. His main research interests include power electronics and motor drives, with more than 100 published IEEE journal and conference papers in this area.

Dr. Jiang was the recipient of five best paper awards in IEEE conferences. He is currently an Associate Editor for IEEE TRANSACTIONS ON INDUSTRY APPLICATIONS.

Xuan Zhao (Graduate Student Member, IEEE) received the B.S. and M.S. degrees in electrical engineering in 2017 and 2020, respectively, from Huazhong University of Science and Technology, Wuhan, China, where he is currently working toward the Ph.D. degree in electrical engineering.

His research interests include multilevel converters, ac motor drive and electromagnetic interference of power electronics system.

Zicheng Liu (Senior Member, IEEE) received the B.S. degree in hydropower engineering from the Huazhong University of Science and Technology (HUST), Wuhan, China, in 2011, and the Ph.D. degree in electrical engineering from Tsinghua University, Beijing, China, in 2016.

During 2014 to 2015, he was a Visiting Student with Purdue University, West Lafayette, IN, USA. During 2016 to 2018, he was a Postdoc Researcher with Beijing Jiaotong University, Beijing, China. He is currently an Associate Professor with HUST. His research interests include multiphase motor control systems and transportation electrification.

Dr. Liu was the recipient of the best letter award for IEEE TRANSACTIONS ON POWER ELECTRONICS, the second-place prize paper award for IEEE JOURNAL OF EMERGING AND SELECTED TOPICS IN POWER ELECTRONICS, and three prize paper awards in IEEE conferences. He is the Vice Chair of IEEE Power Electronics Society Wuhan Chapter.